# Two-Dimensional Ternary Pentagonal BCN: A Promising Photocatalyst Semiconductor for Water Splitting with Strong Excitonic Effects

Mehmet Emin Kilic [*] and Kwang-Ryeol Lee[†]

*Computational Science Research Center, Korea Institute of Science and Technology, Seoul 136-791, Republic of Korea*

Developing photocatalysts that can effectively utilize solar energy to catalyze and decompose water into hydrogen and oxygen is highly desired for sustainable and clean hydrogen energy. Using first-principles calculations, we systematically investigate the structure stability, properties, and possible potential uses of a ternary pentagonal boron carbon nitride ($p$-BCN) monolayer, a recently proposed two-dimensional material. We demonstrate its energetic, dynamical, thermal, and mechanical stability and find it to be stable and dissoluble in liquid water. The monolayer exhibits remarkable mechanical properties, such as high stiffness and ideal strength comparable to its counterparts. Near-zero Poisson's ratio can be tuned to positive and negative (auxetic) values by application of a small strain. The monolayer is semiconducting with a desirable quasidirect band gap of 2.79 eV for efficient visible light absorption, and its valence and conduction bands ideally straddle both the oxidation and reduction potential of water. Our results reveal that in-plane mechanical strain can be utilized to modulate the band-gap and band-edge positions for a better match with the redox potentials of water and solar spectrum. The monolayer has a very high optical absorption coefficient on the order of $10^5$ cm$^{-1}$ in the visible and ultraviolet regions of the solar spectrum. Excitingly, $p$-BCN has distinct excitonic peaks in the visible range with the first exciton binding energy of approximately 1.4 eV. The intrinsic acoustic-phonon-limited carrier mobility of $p$-BCN can reach up to $10^4$ cm$^2$ V$^{-1}$ s$^{-1}$ at room temperature. These theoretical findings imply that $p$-BCN is a promising candidate for optoelectronics, especially as a photocatalyst for water splitting.

## I. INTRODUCTION

Hydrogen as the most abundant element in the universe has the potential for fulfilling future energy demands in our world. Its production, transport, storage, and utilization have emerged as one of the most relevant research subjects [1,2]. Since the pioneering work of Fujishima and Honda [3] in 1972, hydrogen production from water splitting using direct sunlight on semiconductor photocatalysts has become a promising strategy for converting solar energy into clean chemical energy. Great efforts have been made to develop efficient photocatalysts that utilize solar energy to catalyze and decompose water into hydrogen and oxygen [4,5].

In principle, photocatalytic water-splitting reaction using semiconductor-based photocatalysts with sunlight consists of three major steps as illustrated in Fig. 1. Light-driven water splitting is initiated when the semiconductor absorbs photons whose energy exceeds its band-gap energy and creates excited electrons in the conduction band and leaves their opposite charges (holes) in the valence band of the semiconductor. After that, the second step in photocatalytic water splitting involves the separation of photogenerated electron-hole pairs and their migration to the semiconductor surface. The final step of the photocatalytic process is the participation of electrons and holes in the reduction and oxidation reaction. The balance of thermodynamics and kinetics of these three complementary steps determines the overall efficiency of a given photocatalyst [6].

Taking into account the above three steps in the splitting of water on semiconductor photocatalyst, several requirements must be satisfied [7]. Firstly, the band-gap energy of the semiconductor must be higher than 1.23 eV, which is the minimum energy required to split water [8]. Moreover, the photocatalyst should have a narrow band gap ($E_{gap} <$ 3.0 eV) to effectively harvest visible light. For photoexcitation, the photocatalyst should have appropriate band-edge positions for the reduction and oxidation of water to H$_2$ and O$_2$. Such that, the conduction-band edge of the semiconductor photocatalyst must be higher than the potential for hydrogen evolution (H$^+$/H$_2$, $-4.44$ eV at pH $= 0$) while the valence-band edge must be lower than the potential for oxygen evolution (H$_2$O/O$_2$, $-5.67$ eV at pH $= 0$). The efficient charge separation and migration are ascribed by

_____
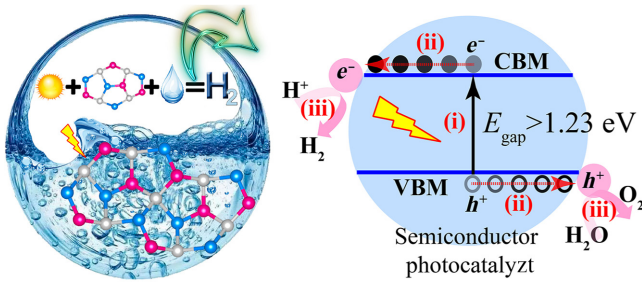[*]mekilic@kist.re.kr
[†]krlee@kist.re.kr

FIG. 1. Schematic illustration of the basic principle of the overall water splitting on a semiconductor photocatalyst.

the low rate of recombination of photogenerated electrons and holes. In this regard, two-dimensional (2D) materials have a small migration distance, which can inhibit the recombination of charges, are more attractive than the use of three-dimensional (3D) semiconductors [5,9]. Furthermore, the large surface area of 2D materials provides much more active sites for the adsorption of $OH^-$, $H^+$, and $H_2O$ participating in the photocatalytic reaction [10]. Remarkably, the electronic properties of 2D materials including the band-gap and band-edge positions can effectively be tuned by strain engineering [11–13], which plays a role in the overall efficiency of the photocatalyst. Hence, the intrinsic properties of 2D materials make them promising candidates for photocatalytic water splitting.

2D metal-free semiconductor photocatalysts have attracted growing attention in recent years for solar-energy conversion by light-induced water splitting and carbon-dioxide reduction [14–16]. Recently, 2D pentagonal materials, including penta-graphene [17] and group-IV carbides [11] have been of great interest due to their unique Cairo tessellation structure, and exotic physical and chemical properties. After the successful experimental synthesis of atomically thin pentagonal $PdSe_2$, having a high air stable behavior with highly anisotropic optical, electrical, and optoelectronic properties [18], 2D materials with pentagonal lattice are considered to be one of the most useful milestones in the field of materials science [19]. In our previous study, we carried out detailed investigations of 2D unitary, binary, and ternary penta-carbides and examined their desirable electronic and optical properties for photocatalytic water splitting [11]. Not only pentagonal materials but also their tetrahexagonal (denoted as *th*) counterparts by Stone-Wales transformation have recently been suggested as a promising photocatalyst for water splitting [12,13,20]. Thus, pentagonal and their tetrahexagonal counterparts are potential candidates as photocatalysts for use in photocatalytic water-splitting applications.

The zero band gap of graphene and wide band gap of hexagonal boron nitride (*h*-BN) limit their applications in photocatalysis. Their intermediates, called ternary BCN compounds, however, are suitable for photocatalytic

water splitting due to their super flexibility in engineering the electronic and optical properties by chemical variations [21]. As for the Cairo-pentagonal-lattice, three phases of pentagonal boron nitride, namely $p$-$B_2N_4$, $p$-$B_4N_2$, and $p$-BN (see Fig. S1 within the Supplemental Material [22]), were theoretically predicted [23,24]. To obtain uniformly distributed threefold coordinated B—N bonds in the pentagonal lattice, fourfold coordinated sites can be occupied by group-IV elements (Si or C). Very recently, Varjovi *et al.* have proposed a ternary pentagonal BNSi ($p$-BNSi) monolayer with high carrier mobility and strong excitonic effects, is of great potential for photocatalytic applications [25]. Zhao *et al.* predicted ternary pentagonal BCN monolayer ($p$-BCN) and showed its dynamical, thermal, and mechanical stability [26]. They performed more detailed studies on its intrinsic piezoelectricity properties. Herein, using first-principles calculations, we investigate the structural stability of $p$-BCN as a benchmark and systematically studied its mechanical, electronic, and optical properties. Besides, considering the potential uses of $p$-BCN, we have also carefully studied its potential to be an efficient photocatalyst semiconductor for water splitting under visible light illumination.

## II. METHOD

The initial structure of the $p$-BCN monolayer is optimized through the density-functional theory (DFT) embedded in the plane-wave Vienna *ab initio* simulation package (VASP) [27]. The generalized gradient approximation (GGA) as parameterized by Perdew, Burke, and Ernzerhof (PBE) for the exchange-correlation interactions was used [28]. To manipulate the electron-core interactions, the projector augmented wave (PAW) method with a plane-wave basis set is used [29,30]. The kinetic energy cutoff is set to 520 eV. The periodic boundary conditions are applied along with the plane directions. To study 2D systems, a vacuum layer of 20 Å is added in the perpendicular-to-the-plane [001] direction ($z$ direction). The irreducible Brillouin zone (BZ) is represented by $32 \times 32 \times 1$ $k$-point meshes for the geometry optimization and electronic structure calculations. Both the geometries and atomic positions are fully relaxed until the energy convergence criterion and stress force acting on each atom are less than $10^{-5}$ eV and $10^{-3}$ eV/Å, respectively. As the GGA PBE usually underestimates the electronic band gaps, the corrected electronic band structures are calculated by adopting the hybrid Heyd-Scuseria-Ernzerhof (HSE06) method [31]. Moreover, we employ the $GW_0$ approach on the basis of the PBE functional to obtain the quasiparticle (QP) band gap [32]. To further investigate the dynamical stability, the lattice dynamics calculations are performed by using the Phonopy code [33], where a $7 \times 7 \times 1$ supercell composed of 294 atoms is used. To examine the thermal stability and structural stability in liquid water, *ab initio*
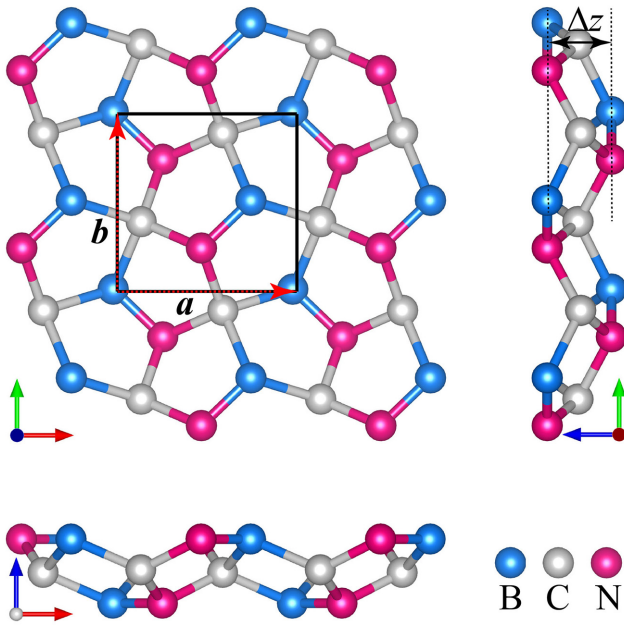
FIG. 2. Top and side views of optimized atomic structure of *p*-BCN. Blue, silver, and pink balls represent B, C, and N atoms, respectively. The unit cell is marked by a black line and **a** and **b** lattice vectors are illustrated by red dashed arrows on the unit cell.

molecular dynamics (AIMD) simulations are carried out under *NVT* ensemble where the temperature is controlled using a Nose-Hover thermostat [34,35] and a time step of 1 fs is used.

## III. RESULTS AND DISCUSSIONS

### A. Structure characterization and stability

The optimized atomic structure of *p*-BCN is demonstrated in Fig. 2. The structure is composed entirely of pentagonal rings. The unit cell (marked by the black line) contains six atoms with B:C:N ratio of 1:1:1. Each carbon atom is fourfold coordinated and binds to threefold coordinated B and N atoms. The fully relaxed lattice constants are $a = 3.670$ Å and $b = 3.632$ Å. The calculated average B—N bond length in *p*-BCN (about 1.406 Å) is in between hexagonal BN (about 1.451 Å) and tetrahexagonal BN (about 1.355 Å) [36]. The B—C and C—N bond lengths are found to be $d_{BC} = 1.631$ Å and $d_{CN} = 1.498$ Å, respectively. The buckling thickness $\Delta z$ (depicted in Fig. 2) is 1.312 Å. All these obtained lattice parameters agree very well with those by Zhao *et al.* [26].

We now examine the energetic, dynamical, thermal, and mechanical stability of *p*-BCN. First of all, we investigate the energetic stability by calculating the cohesive energy, defined as $E_{coh} = \sum n_{atom}E_{atom} - E_{BCN})/(n_B + n_C + n_N)$ where $E_{atom}$ denotes the energy of a single isolated atom and $n_{atom}$ denotes the number of atoms contained in the

unit cell. $E_{BCN}$ denotes the total energy of the *p*-BCN monolayer. We calculate the cohesive energy of *p*-BCN as 6.18 eV per atom, which is comparable with well-known 2D materials including phosphorene (3.48 eV per atom) [37], arsenene (2.99 eV per atom) [38], and antimonene (2.87 eV per atom) [39]. We further calculate the energy difference ($\Delta E$) between *p*-BCN and its hexagonal counterparts (graphene and *h*-BN). The $\Delta E$ of *p*-BCN about 1204 meV per atom is relatively higher than that of penta-graphene (*p*-C) about 902 meV per atom (obtained from graphene) and graphdyine about 823 meV per atom experimentally synthesized on the copper surface [40]. We note that such a relatively high formation energy suggests that *p*-BCN can be synthesized on suitable substrates, which may reduce the formation energy sufficiently to thermodynamically stabilize the monolayer.

To examine the dynamical stability of *p*-BNC, we carry out lattice dynamics phonon calculations. As presented in Fig. 3(a), there is no imaginary frequency in the phonon dispersion curves, thus confirming its dynamic stability. According to the atom-projected phonon density of states (PhDOS), we observe that the highest phonon frequencies come from the vibration of B and N atoms rather than that of C, which is mainly attributed to the strong B—N bonds. Moreover, the highest phonon frequency of 1363 cm$^{-1}$ at $\Gamma$ point in *p*-BCN is comparable with that in other 2D pentagonal structures including penta-graphene (*p*-C) (1632 cm$^{-1}$), *p*-SiC$_2$ (1464 cm$^{-1}$), *p*-GeC$_2$ (1497 cm$^{-1}$), and *p*-SnC$_2$ (1476 cm$^{-1}$) [11], suggesting a strong bond network in the *p*-BCN monolayer.

Next, we examine the phonon instability known as Kohn anomaly [41] in *p*-BCN that is expected to occur behind the elastic instability. In the next section, we discuss the ideal strength of the *p*-BCN monolayer and reveal strain points at which the monolayer completely loses its stiffness and thereby breaks (endpoint of the prefailure stress-strain curve). Turning our focus to the phonon instability, we perform the lattice dynamics calculations for the strained *p*-BCN monolayer. The phonon dispersion spectra under isotropic in-plane strain (equibiaxial strain) up to 16.2% is demonstrated in Fig. 3(b). The first thing to note is that there is no appreciable negative frequency in the phonon dispersion curve at 16.0% strain, indicating that the structure of *p*-BCN still maintains its dynamical stability up to this strain. As the softening phonon modes, mainly attributed from the vibration of B—C and N—C bonds, are much more sensitive to displacements, the small imaginary frequency emerges in the phonon spectrum when the strain goes beyond 16.0% strain (e.g., 16.2% strain), and thus phonon instability occurs. We note that the phonon instability in *p*-BCN does not precede the elastic instability, and thus may limit the ideal strength of the monolayer. The first occurrence of phonon instability in *p*-BCN is 2 times more than that in *p*-BN (6.2% biaxial strain), *p*-BN$_2$ (7.8%) [24]. Consequently, good dynamic stability even
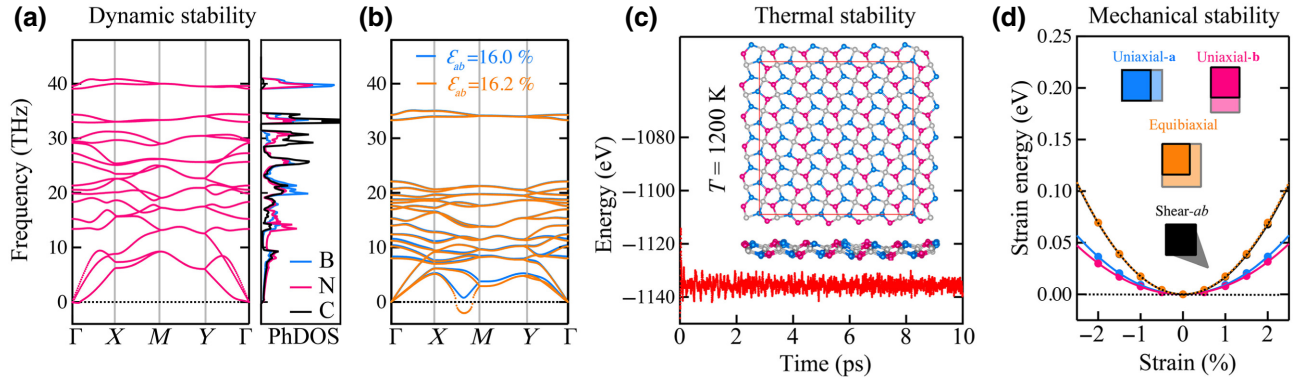
FIG. 3. (a) Phonon-band dispersion with atom-projected phonon density of states (PhDOS). (b) Phonon-band dispersions at the extreme of equibiaxial strain. (c) Variation of potential energy with respect to time for 10 ps at $T = 1200$ K where the atomic configurations at the end of the simulation is depicted in the inset. (d) Variation of strain energy with respect to various deformations (uniaxial, biaxial, and shear strains) depicted in the inset. The energy at the equilibrium state is set to zero.

under large external strain makes the $p$-BCN monolayer a prominent material for its potential applications.

We further investigate the thermal stability of $p$-BCN by performing the AIMD simulations at various temperatures (300–1500 K) for 10 ps (Fig. S2 within the Supplemental Material [22]). We observe that the monolayer can withstand temperatures as high as 1200 K [Fig. 3(c)]. The time-dependent evolution of energy, which oscillated within a very narrow range (approximately 0.1 eV/atom at 1200 K) during the entire AIMD simulation, and the atomic configuration at the end of the AIMD simulations (inset) at which neither geometric reconstruction nor bond breaking, are observed, confirm the thermal stability of $p$-BCN.

Next, we investigate the structural stability of $p$-BCN in liquid water to show its practical applications in photocatalytic water splitting. We place a $3 \times 3 \times 1$ supercell of the $p$-BCN monolayer in liquid water with a fixed density of 1 g/cm$^3$ (231 atoms are used in the $NVT$ ensemble), and the system is thermally equilibrated at 300 K for 10 ps. The results show that the monolayer would be stable and indissoluble in liquid water at room temperature (Fig. S3 within the Supplemental Material [22]). From the snapshot at the end of AIMD simulations, we observe that water molecules are spontaneously dissociated into OH$^-$ and H$^+$ radicals on the $p$-BCN monolayer (where the OH and H molecules are located at the top of B and N atoms, respectively) without any energy barrier, which is significant for the photocatalytic reactions on the surface.

We finally examine the mechanical stability of $p$-BCN by evaluating the elastic stability criteria [42] as $C_{11}C_{22} - C_{12}^2 > 0$ and $C_{66} > 0$ where $C_{11}$, $C_{22}$, $C_{12}$, and $C_{66}$ are the independent elastic constants. The corresponding elastic constants $C_{ij}$ can be obtained from the second order derivatives of the strain energy with respect to in-plane strain via $C_{ij} = \partial^2 E_s / \partial \varepsilon_{ij}^2 / S_0$ where $E_s$, $\varepsilon_{ij}$, and $S_0$ are the strain energy, corresponding strains (compressive and tensile),

and area of the equilibrium supercell, respectively. For more details refer to Ref. [20]. The uniaxial strain along the **a** lattice direction is defined as $\varepsilon_{11} = a' - a/a$ where $a$ and $a'$ are the lattice constant of the unstrained and strained supercells, respectively. The **b** lattice direction is fully relaxed when the uniaxial strain is applied along the **a** lattice direction. The variation of strain energy with respect to various deformations (uniaxial, biaxial, and shear strains) is plotted in Fig. 3(d). The calculated elastic constants of $C_{11} = 219.2$ N/m, $C_{22} = 184.7$ N/m, $C_{12} = 3.7$ N/m, $C_{66} = 104.2$ N/m meet the elastic stability criteria. To summarize, we reveal that $p$-BCN possesses robust stability by evaluating the energetic, dynamical, thermal, and mechanical stability, suggesting the possibility to fabricate the $p$-BCN monolayer experimentally.

### B. Mechanical properties

After revealing the good stability of $p$-BCN, we investigate its mechanical properties such as Young's modulus, Poisson's ratio, and ideal strength. We start with exploring the direction dependent mechanical response in $p$-BCN by calculating the orientation-dependent in-plane Young's modulus $Y^{2D}(\theta)$ and Poisson's ratio $\nu(\theta)$ using the following expressions [43]:

$$Y^{2D}(\theta) = \frac{C_{11}C_{22} - C_{12}^2}{C_{11}s^4 + C_{22}c^4 + \left(\frac{(C_{11}C_{22} - C_{12}^2)}{C_{66}} - 2C_{12}\right)s^2c^2},$$
(1)

$$\nu(\theta) = \frac{C_{12}(s^4 + c^4) - \left(C_{11} + C_{22} - \frac{(C_{11}C_{22} - C_{12}^2)}{C_{66}}\right)s^2c^2}{C_{11}s^4 + C_{22}c^4 + \left(\frac{(C_{11}C_{22} - C_{12}^2)}{C_{66}} - 2C_{12}\right)s^2c^2},$$
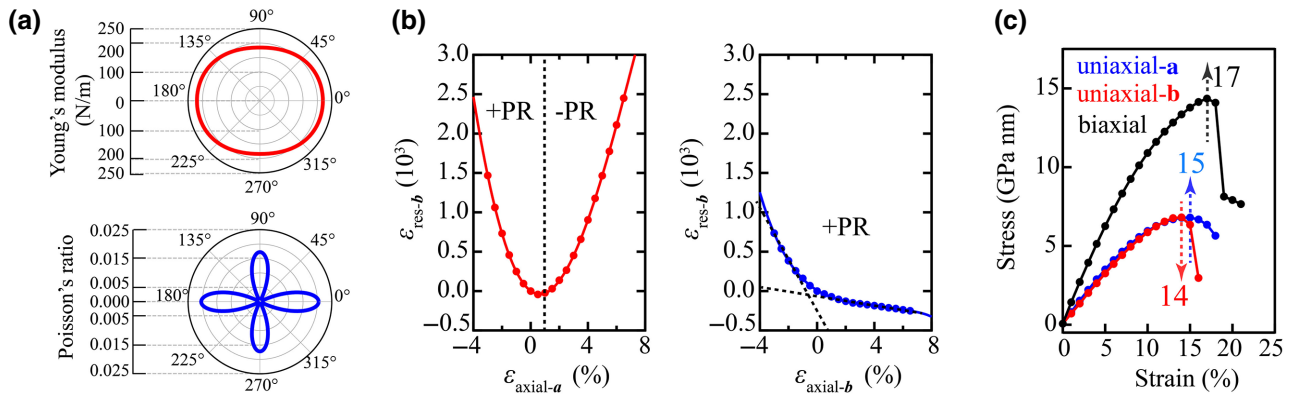(2)

FIG. 4. (a) Polar diagram of Young's modulus (upper panel) and Poisson's ratio (lower panel). (b) Variation of response strain perpendicular to applied axial strain along the **a** and **b**. (c) Stress-strain curve for uniaxial-**a**, uniaxial-**b**, and equibiaxial strains.

where $s = \sin(\theta)$, and $c = \cos(\theta)$. As shown in Fig. 4(a), Young's modulus and Poisson's ratio of $p$-BNC are anisotropic. Such that, the maximum Young's modulus is located along the **a** lattice direction as $Y_{\mathbf{a}}^{2D} = 220$ N/m whereas the minimum is located along the **b** direction as $Y_{\mathbf{b}}^{2D} = 185$ N/m, agreeing well with the previous report [26]. Young's modulus of $p$-BCN is much higher than that of $p$-BN (133.67 N/m) [24] and close to $p$-BN$_2$ (224.18 N/m) [24], $th$-BN (232.39 N/m) [36], and $h$-BN (271 N/m) [44]. As for Poisson's ratio (PR), contrary to penta-graphene having near-zero negative PR ($-0.07$) [11,17], the $p$-BCN monolayer exhibits a near-zero positive PR with the value of 0.02 along the **a** and **b** lattice directions. As PR is defined as the ratio of response strain to the applied longitudinal strain, such near-zero PR might be attractive in various applications, especially where changes in the lateral dimensions are detrimental to a system's performance.

We further investigate the mechanical response behavior through the application of large uniaxial strain ranging from $-4$ to 10% along the **a** and **b** lattice directions using a $2 \times 2 \times 1$ supercell. The variation of response strain perpendicular to the applied uniaxial strain is presented in Fig. 4(b). It can be seen that the response strain ($\varepsilon_{\text{res}-b}$) decreases with the increase of uniaxial strain from $-4$ up to 1.0% applied along the **a** lattice direction ($\varepsilon_{\text{axial}-a}$), which is not surprising since PR is positive. Subsequently, with further strain, auxetic behavior in $p$-BCN starts to take place as the response strain increases. Thus, the sign of PR is changed from positive to negative at 1.0% uniaxial strain applied along the **a** lattice direction. On the other hand, the response strain ($\varepsilon_{\text{res}-a}$) always decreases with the increase of uniaxial strain ($\varepsilon_{\text{axial}-b}$) applied along the **b** lattice direction. Our results show that $p$-BCN can display positive and negative PR when uniaxial strain is applied along the **a** lattice direction while positive PR along the **b** lattice direction. Thus, $p$-BCN is multifunctional material and can be considered as an auxetic, nonauxetic, and partially auxetic (a negative PR in a certain direction) monolayer, depending on the choice of the direction of the applied stretching.

Next, we study the ideal strength, which is the maximum stress that the material can withstand while being elongated, stretched, or pulled before breaking. We determine the ultimate tensile strength representing the highest point on the stress-strain curve. We plot the stress-strain curves of $p$-BCN using a $3 \times 3 \times 1$ supercell in Fig. 4(c). The ultimate tensile strength values are found to be 11.6 GPa.nm, 12.7 GPa.nm, and 15.7 GPa.nm for uniaxial-**a**, uniaxial-**b**, and equibiaxial strains at which the corresponding strains, namely ultimate tensile strains (UTS) are about 15%, 14%, and 17%, respectively. For equibiaxial strain, the UTS$_{\text{ab}}$ in $p$-BCN is higher than that in $p$-BN and $p$-BN$_2$ (12%) [24], relatively lower than that in $p$-C (21%) [11], and much more lower than that in $th$-BN (27%) [36]. Thus, $p$-BCN can withstand very large deformations, allowing to use strain to tune its properties for specific applications.

## C. Electronic properties

To understand the electronic nature of $p$-BCN, we calculate the electronic band structure, atom and orbital projected density of states (pDOS), and band-decomposed charge distributions, and the results are plotted in Fig. 5. It can be seen that the $p$-BCN monolayer is semiconducting with a quasidirect band gap of 2.79 eV at the HSE06 method (1.71 eV at the PBE functional), agreeing well the previous report as 2.81 eV [26]. The valance-band maximum (VBM) and conduction-band minimum (CBM) are located at the $\Gamma$-$X$ point in the BZ. From the pDOS, the $p_z$ orbitals of B atoms have a considerable contribution to CBM while the $p$ orbitals of B, C, and N atoms, dominantly N-$p_z$ provide the main contribution to VBM, which are also confirmed by the band-decomposed charge-density distribution of VBM and CBM.
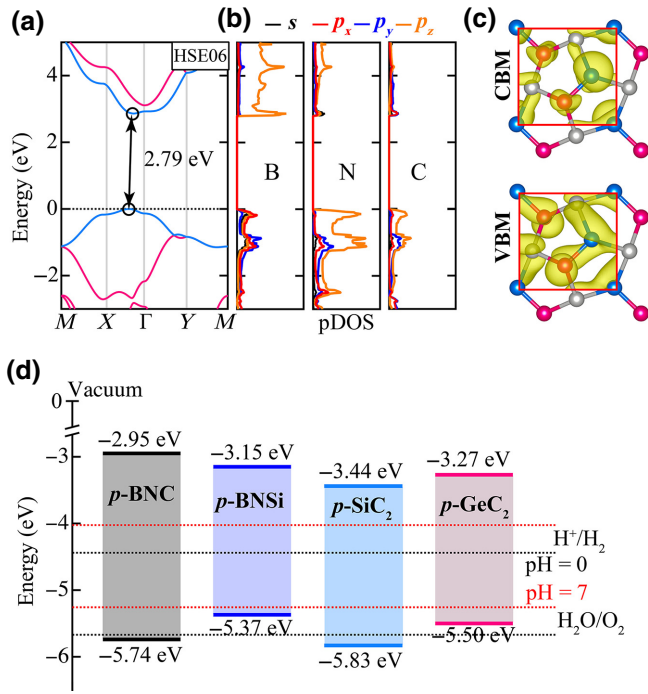
FIG. 5. (a) Electronic band structure of $p$-BCN at the HSE06 method. The Fermi energy (black dashed line) is aligned to VBM and set to 0 eV. The energy bands close to the Fermi energy are illustrated in sky-blue color. (b) Atom- and orbital-projected density of states where the $s$, $p_x$, $p_y$, and $p_z$ orbitals of B, C, and N atoms are in black, red, blue, and orange, respectively. (c) Band-decomposed charge density of VBM and CBM with the isosurface value of 0.01 e$\text{Å}^3$. (d) The energy level of VBM and CBM calculated at the HSE06 method with respect to vacuum level (which is set to 0 eV) for $p$-BCN and other pentagonal structures ($p$-BNSi [25], $p$-SiC$_2$ [11], and $p$-GeC$_2$ [11]) for the comparison. The redox potentials of water splitting are marked by the dashed line at pH = 0 (black) and pH = 7 (red) as shown for comparison.

To assess the possibility of using the $p$-BCN monolayer as a photocatalyst semiconductor, we further evaluate its electronic properties for photocatalytic water-splitting reaction. The band-gap energy of $p$-BCN (2.79 eV) exceeds the free energy of water splitting (1.23 eV) and is in favor of harvesting visible light as lower than 3.0 eV. Besides, we calculate the band-edge positions of $p$-BCN with reference to the vacuum energy, which we extract from the local potential distribution within the unit cell. The band-edge energies with respect to water redox potentials from the HSE06 method are plotted in Fig. 5(d). The energy level of CBM ($-2.95$ eV) is higher than the hydrogen reduction potential of water while that of VBM ($-5.74$ eV) is lower than the oxidation potential of water at pH = 0. Hence, the band-edge positions of $p$-BCN are thermodynamically favorable for water splitting. We note that the position of VBM only lies 0.07 eV below the oxidation reaction potential to drive the redox reactions at

pH = 0, which may result in a low activity for the water-splitting reaction. In this respect, the $p$-BCN monolayer has an adequate driving force to split water into hydrogen and oxygen at pH > 0. Thus, the band-gap energy and band-edge positions of $p$-BCN indicate its great potential for overall water splitting.

As strain engineering is an effective way to improve the intrinsic properties of 2D materials [11,19,36,45,46], we further investigate the effect of external strain on the electronic properties of $p$-BCN. Figure 6 shows the variation of band-gap energy and band-edge positions of $p$-BCN with respect to uniaxial strain applied along the **a** lattice direction (denoted as uniaxial-**a**) and equibiaxial strain at the HSE06 method. For uniaxial-**a**, the CBM position pronouncedly shifts downward with the increase of tensile strain while the energy level of VBM is nearly unchanged up to 12% tensile strain, and then upward, resulting in the decrease of band-gap energy. As for equibiaxial strain, the CBM and what is more VBM positions shift downward gradually with the increase of strain. Remarkably, the band-edge positions in $p$-BCN can be adjusted to more suitable places for water-splitting reaction by equibiaxial strain. Moreover, the band-gap energy increases with compression strains whereas slightly decreases with the increase of tensile strain. Hence, the band edge and band gap of $p$-BCN can effectively be modulated by strain engineering, which could facilitate its utilization in photocatalytic water splitting.

Next, we examine the carrier effective mass and mobility of the $p$-BCN monolayer. Firstly, we calculate the effective mass of electrons ($m_e^*$) and holes ($m_h^*$) by fitting the CBM and VBM respectively, to parabolic functions using $m^* = \hbar^2 [\partial^2 E(k)/\partial k^2]^{-1}$ where $E(k)$ is the corresponding band-edge energy as a function of wave vector $k$ and $\hbar$ is the reduced Plank constant. The effective mass of electron along the **a** and **b** lattice directions is calculated as 0.42 $m_0$ and 0.46 $m_0$ while that of hole is 0.80 $m_0$ and 0.50 $m_0$ ($m_0$ is free electron mass), respectively. Next, we study the carrier mobility ($\mu$) of $p$-BCN along the $i$ transport direction in the framework of deformation potential (DP) theory using the following equation [47]:

$$\mu_i = \frac{e\hbar^3 \left(\frac{5C_i + 3C_j}{8}\right)}{k_B T (m_i^*)^{3/2}(m_j^*)^{1/2} \left(\frac{9E_{d,i}^2 + 7E_{d,i}E_{d,j} + 4E_{d,j}^2}{20}\right)}, \quad (3)$$

where $i \perp j$ and $E_d$ is the DP constant defined as the first derivative of energy shift ($\Delta E$) of the VBM and CBM with respect to lattice deformation ($\Delta l/l_0$) ($l_0$ is the lattice of optimized unstrained supercell). We calculate the DP constant under very small uniaxial strains from $-1$ to 1% with the increment of 0.5% along the **a** and **b** lattice directions. We plot the $\Delta E$ versus $\Delta l/l_0$ in Fig. S4 within the Supplemental Material [22] at which the slope of the linear fit
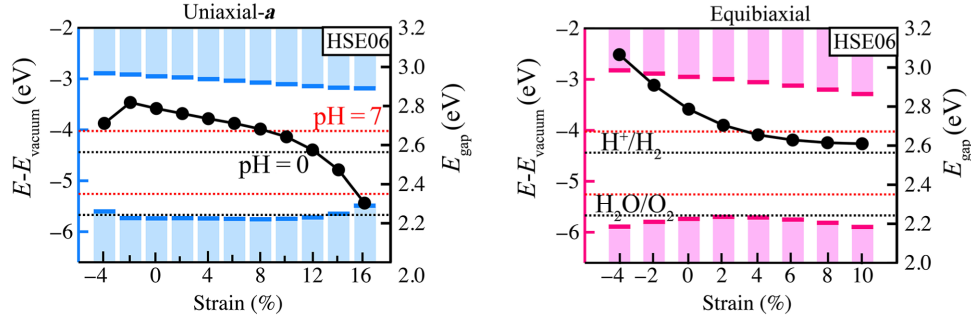
FIG. 6. Variation of band-edge locations with respect to the vacuum level (which is set to zero), and band-gap energies versus uniaxial-**a** and equibiaxial strains. The redox potentials of water splitting are marked by the dashed line at pH = 0 (black) and pH = 7 (red) as shown for comparison.

data gives the DP constants. We find that the DP constant of the electron (1.39 and 1.66 eV) is larger than that of the hole (0.52 and 1.59 eV) along the **a** and **b** lattice directions, respectively. This indicates that the coupling strength of electron to the acoustic phonon is stronger than that of the hole. Particularly, electrons are more strongly scattered by the acoustic phonons than holes in the **a** lattice direction. We further calculate the carrier mobility of electrons and holes along the **a** and **b** transport directions at 300 K and the obtained results are summarized in Table I. The carrier mobility of electron is calculated as $1.08 \times 10^4$ and $0.85 \times 10^4$ cm$^2$ V$^{-1}$ s$^{-1}$ along the **a** and **b** lattice directions, respectively. Moreover, the hole mobility is about $0.96 \times 10^4$ and $0.91 \times 10^4$ cm$^2$ V$^{-1}$ s$^{-1}$ along the **a** and **b** lattice directions, respectively. Thus, the carrier mobility of $p$-BCN in the order of $10^4$ cm$^2$ V$^{-1}$ s$^{-1}$ is comparable with that in graphene ($3.39 \times 10^5$ and $3.22 \times 10^5$ cm$^2$ V$^{-1}$s$^{-1}$ for electron and hole, respectively), silicene ($2.57 \times 10^5$ and $2.22 \times 10^5$ cm$^2$ V$^{-1}$ s$^{-1}$ for electron and hole) [48]. Thus, the photogenerated carriers can fast transfer within $p$-BCN, which is desirable for the photocatalytic water-splitting reaction process.

### D. Optical properties

To examine the solar-energy utilization of $p$-BCN as a solar-driven catalyst, we study its optical properties. By including many-body effects using $GW$ approximation, we calculate the optical absorption coefficient $\alpha(\omega)$ based on

the dielectric function using the following formula [49]:

$$\alpha(\omega) = \sqrt{2}\omega\left[\sqrt{\varepsilon_1^2(\omega) - \varepsilon_2^2(\omega)} - \varepsilon_1(\omega)\right]^{1/2}, \quad (4)$$

where $\varepsilon_1$ and $\varepsilon_2$ are the real and imaginary parts of dielectric function, respectively. By employing a single-shot $GW$ method ($GW_0$), we obtain the QP energies. The QP band gap is found to be 3.71 eV, which is 0.92 eV higher than the electronic band gap obtained from the HSE06 method. We carry out the optical absorption coefficient with the imaginary part of the dielectric function within the random phase approximation (RPA) [50] on the top of $GW_0$. As shown in Fig. 7, the optical absorption peaks are in the UV region without excitonic effects since electron-electron interactions are only taken into account and electron-hole interactions neglected in the $GW_0$-RPA method. However, as electron-hole pairs are created on semiconductors under illumination during the photocatalytic process, it is worthwhile to include their interactions (electron-hole) and excitonic effects in the optical spectrum of $p$-BCN. In this respect, we calculate the optical absorption spectrum by employing the Bethe-Salpeter equation (BSE) [51] on top of the $GW_0$, where both electron-electron and electron-hole interactions are included. Upon inclusion of electron-hole interactions within the $GW_0$+BSE, it is observed that the optical spectra is greatly modified (i.e., redshift in the optical spectra). This shows that electron-hole interactions significantly dominate the optical spectrum of $p$-BCN. The prominent optical absorption peaks emerge in the visible

TABLE I. Predicted charge-carrier mobility of $p$-BCN[a].

| | $m_{\mathbf{a}}^*/m_0$ | $m_{\mathbf{b}}^*/m_0$ | $C_{\mathbf{a}}$ ($C_{11}$) | $C_{\mathbf{b}}$ ($C_{22}$) | $E_{d,\mathbf{a}}$ | $E_{d,\mathbf{b}}$ | $\mu_{\mathbf{a}}$ | $\mu_{\mathbf{b}}$ |
|---|---|---|---|---|---|---|---|---|
| Electron | 0.42 | 0.46 | 219.2 | 184.7 | 1.39 | 1.66 | $1.08 \times 10^4$ | $0.85 \times 10^4$ |
| Hole | 0.80 | 0.50 | 219.2 | 184.7 | 0.52 | 1.59 | $0.96 \times 10^4$ | $0.91 \times 10^4$ |

[a] $m_a^*$ and $m_b^*$ are the carrier effective mass along $\Gamma$-**a** and $\Gamma$-**b** directions, respectively. $m_0$ is the mass of free electron. $C_{\mathbf{a}}$ and $C_{\mathbf{b}}$ are the elastic stiffness constants in the unit of N/m. $E_{d,\mathbf{a}}$ and $E_{d,\mathbf{b}}$ are the deformation potential constants in eV. $\mu_{\mathbf{a}}$ and $\mu_{\mathbf{b}}$ are carrier mobility in cm$^2$ V$^{-1}$ s$^{-1}$ at $T$ = 300 K.
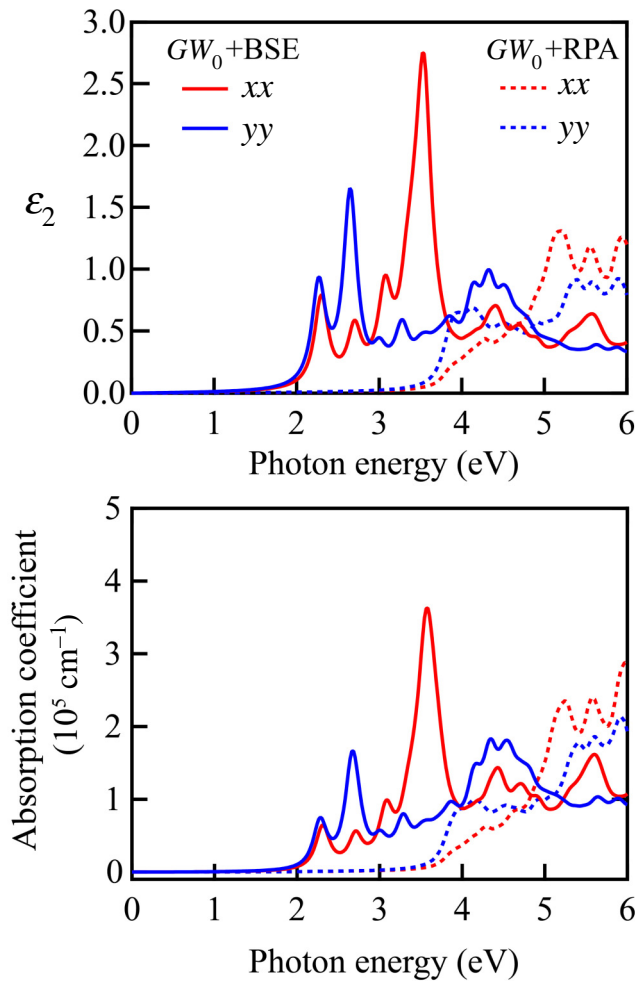
FIG. 7. Imaginary part ($\varepsilon_2$) of the dielectric functions (upper panel) and optical absorption coefficient (lower panel) of $p$-BCN for light polarization parallel to its axis by the $GW_0$+RPA (dashed lines) and $GW_0$+BSE (solid lines) approaches. The Gaussian broadening is adopted for 0.05 eV.

and ultraviolet regions with high optical absorption coefficients (approximately $10^{-5}$ cm$^{-1}$), which can be comparable to those of perovskite solar cells [52]. The high optical response in the visible-UV regime makes $p$-BCN promising for photocatalytic water splitting. Remarkably, the distinct optical absorption peaks below the QP $GW_0$ gap, which are utterly missing in the $GW_0$+RPA, are observed. These obvious peaks indicate the strong quantum confinement effect in the $p$-BCN monolayer and correspond to the strongly bound excitons. The excitonic binding energy of the lowest energy exciton is defined as the difference between the QP band-gap energy and the exciton energy using $GW_0$ and $GW_0$+BSE methods, respectively. The first absorption peak occurring at 2.26 eV is due to exciton absorption. Thus, the binding energy of the first exciton is estimated to be 1.45 eV, which is higher than that of many MXenes [53] and smaller than 2D graphane (about

1.6 eV), GeC (about 1.82 eV) [54], and BN (about 2.1 eV). The large binding energy of $p$-BCN is due to the large QP band-gap energy of 3.70 eV and thus less Coulomb screening. The obvious excitonic absorption peaks indicate the strong quantum confinement effect in $p$-BCN. Therefore, the strong optical absorption capability in the visible region and remarkable excitonic effects in $p$-BCN confirm the applications of efficient light harvesting in optoelectronic device.

## IV. CONCLUSION

We investigate the stability, properties, and potential application of the $p$-BCN monolayer by first-principles calculations. Firstly, we verify its energetic, dynamical, thermal, and mechanical stability with the structure stability and dissolubility in liquid water at room temperature. Next, we systematically study its mechanical, electronic, and optical properties.

(a) The analysis of mechanical properties show that the monolayer exhibits direction-dependent Young's modulus, Poisson's ratio, and ultimate tensile strength. Due to the sign-tunable Poisson's ratio, the monolayer can be considered as nonauxetic, auxetic, and partially auxetic (a negative PR in certain direction) material, depending on the choice of the direction of the applied stretching. Thus, the $p$-BCN monolayer has great potential to be a multifunctional material for nanomechanical applications.

(b) The analysis of electronic properties revealed that the monolayer is semiconducting with a quasidirect band gap of 1.71, 2.79, and 3.71 eV at the PBE, HSE06, and $GW_0$ methods, respectively. The monolayer has appropriate band-edge positions that perfectly meet the requirements of photocatalytic water splitting. The band-gap and band-edge positions can be modulated by strain engineering. The monolayer has small carrier effective mass and high mobility (approximately $10^4$ cm$^2$V$^{-1}$s$^{-1}$).

(c) The analysis of optical properties examined that the monolayer has high optical absorption capability in the visible region ($\sim 10^5$ cm$^{-1}$) with remarkable excitonic effects, which are a big advantage for its utilization as a water-splitting catalyst.

All these findings suggest that the $p$-BCN monolayer has advantages for various applications, including nanoelectronics, optoelectronics, and particularly potential as a visible-light-driven water-splitting photocatalyst.

[1] W. Lubitz and W. Tumas, Hydrogen: An overview, Chem. Rev. **107**, 3900 (2007).

[2] G. Li, H. Kobayashi, J. M. Taylor, R. Ikeda, Y. Kubota, K. Kato, M. Takata, T. Yamamoto, S. Toh, and S. Matsumura, Hydrogen storage in Pd nanocrystals covered with a metal–organic framework, Nat. Mater. **13**, 802 (2014).

[3] A. Fujishima and K. Honda, Electrochemical photolysis of water at a semiconductor electrode, Nature **238**, 37 (1972).

[4] D. K. Lee and K.-S. Choi, Enhancing long-term photostability of $BiVO_4$ photoanodes for solar water splitting by tuning electrolyte composition, Nat. Energy **3**, 53 (2018).

[5] T. Takata, J. Jiang, Y. Sakata, M. Nakabayashi, N. Shibata, V. Nandal, K. Seki, T. Hisatomi, and K. Domen, Photocatalytic water splitting with a quantum efficiency of almost unity, Nature **581**, 411 (2020).

[6] S. Bai, J. Jiang, Q. Zhang, and Y. Xiong, Steering charge kinetics in photocatalysis: Intersection of materials syntheses, characterization techniques and theoretical simulations, Chem. Soc. Rev. **44**, 2893 (2015).

[7] J. Ran, J. Zhang, J. Yu, M. Jaroniec, and S. Z. Qiao, Earth-abundant cocatalysts for semiconductor-based photocatalytic water splitting, Chem. Soc. Rev. **43**, 7787 (2014).

[8] J. R. Bolton, S. J. Strickler, and J. S. Connolly, Limiting and realizable efficiencies of solar photolysis of water, Nature **316**, 495 (1985).

[9] Y. Li, C. Gao, R. Long, and Y. Xiong, Photocatalyst design based on two-dimensional materials, Mater. Today Chem. **11**, 197 (2019).

[10] Y. Jiang, Z. Liu, S. Guo, L. Wang, Y. Li, and X. Hu, Collaborative compromise of two-dimensional materials in sodium ion capacitors: Mechanisms and designing strategies, J Mater. Chem. A **9**, 8129 (2021).

[11] M. E. Kilic and K.-R. Lee, Penta carbides: Two-dimensional group-IV semiconductors containing C2 dimers for nanoelectronics and photocatalytic water splitting, Phys. Rev. Mater. **5**, 065404 (2021).

[12] M. E. Kilic and K.-R. Lee, Auxetic, flexible, and strain-tunable two-dimensional $th$-AlN for photocatalytic visible light water splitting with anisotropic high carrier mobility, J. Mater. Chem. C **9**, 4971 (2021).

[13] M. E. Kilic and K.-R. Lee, Tetrahex carbides: Two-dimensional group-IV materials for nanoelectronics and photocatalytic water splitting, Carbon **174**, 368 (2021).

[14] H. Dong, S. Hong, P. Zhang, S. Yu, Y. Wang, S. Yuan, H. Li, J. Sun, G. Chen, and C. Li, Metal-free Z-scheme 2D/2D VdW heterojunction for high-efficiency and durable photocatalytic $H_2$ production, Chem. Eng. J. **395**, 125150 (2020).

[15] H. Xu, X. She, T. Fei, Y. Song, D. Liu, H. Li, X. Yang, J. Yang, H. Li, and L. Song, Metal-oxide-mediated subtractive manufacturing of two-dimensional carbon nitride for high-efficiency and high-yield photocatalytic $H_2$ evolution, ACS Nano **13**, 11294 (2019).

[16] L. Lin, Z. Yu, and X. Wang, Crystalline carbon nitride semiconductors for photocatalytic water splitting, Angewandte Chemie **131**, 6225 (2019).

[17] S. Zhang, J. Zhou, Q. Wang, X. Chen, Y. Kawazoe, and P. Jena, Penta-graphene: A new carbon allotrope, Proc. Nat. Acad. Sci. **112**, 2372 (2015).

[18] A. D. Oyedele, S. Yang, L. Liang, A. A. Puretzky, K. Wang, J. Zhang, P. Yu, P. R. Pudasaini, A. W. Ghosh, and Z. Liu, PdSe2: pentagonal two-dimensional layers with high air stability for electronics, J. Am. Chem. Soc. **139**, 14090 (2017).

[19] M. E. Kilic and K.-R. Lee, Four-penta-graphenes: Novel two-dimensional fenestrane-based auxetic nanocarbon allotropes for nanoelectronics and optoelectronics, Carbon **195**, 154 (2022).

[20] M. E. Kilic, S. E. Rad, and S. Jahangirov, Two-dimensional tetrahexagonal $CX_2$ ($X$ = P, As, Sb) semiconductors for photocatalytic water splitting under visible light, Phys. Rev. Mater. **6**, 035402 (2022).

[21] C. Huang, C. Chen, M. Zhang, L. Lin, X. Ye, S. Lin, M. Antonietti, and X. Wang, Carbon-doped bn nanosheets for metal-free photoredox catalysis, Nat. Commun. **6**, 1 (2015).

[22] See Supplemental Material at http://link.aps.org/supplemental/10.1103/PhysRevApplied.18.014066 for additional details on atomic structure of $p$-BCN and its C and BN domains in pentagonal lattice; snapshots of atomic structure of $p$-BCN with AIMD simulations at various temperatures from 300 to 1500 K; atomic configurations and variation of total potential energy with respect to the AIMD time for $p$-BCN in liquid water at 300 K for 10 ps; deformation potential constants.

[23] M. Yagmurcukardes, H. Sahin, J. Kang, E. Torun, F. M. Peeters, and R. T. Senger, Pentagonal monolayer crystals of carbon, boron nitride, and silver azide, J. Appl. Phys. **118**, 104303 (2015).

[24] J. Li, X. Fan, Y. Wei, and G. Chen, Penta-BxNy sheet: a density functional theory study of two-dimensional material, Sci. Rep. **6**, 1 (2016).

[25] M. J. Varjovi, M. E. Kilic, and E. Durgun, Ternary pentagonal BNSi monolayer: Two-dimensional structure with potentially high carrier mobility and strong excitonic effects for photocatalytic applications, Phys. Rev. Mater. **6**, 034004 (2022).

[26] K. Zhao, Y. Guo, Y. Shen, Q. Wang, Y. Kawazoe, and P. Jena, Penta-BCN: A new ternary pentagonal monolayer with intrinsic piezoelectricity, J. Phys. Chem. Lett. **11**, 3501 (2020).

[27] G. Kresse and J. Hafner, Norm-conserving and ultrasoft pseudopotentials for first-row and transition elements, J. Phys. Condens. Matter **6**, 8245 (1994).

[28] J. P. Perdew, K. Burke, and M. Ernzerhof, Generalized Gradient Approximation Made Simple, Phys. Rev. Lett. **77**, 3865 (1996).

[29] P. E. Blöchl, Projector augmented-wave method, Phys. Rev. B **50**, 17953 (1994).

[30] G. Kresse and D. Joubert, From ultrasoft pseudopotentials to the projector augmented-wave method, Phys. Rev. B **59**, 1758 (1999).

[31] J. Heyd, G. E. Scuseria, and M. Ernzerhof, Hybrid functionals based on a screened coulomb potential, J. Chem. Phys. **118**, 8207 (2003).

[32] M. Shishkin and G. Kresse, Self-consistent $GW$ calculations for semiconductors and insulators, Phys. Rev. B **75**, 235102 (2007).

[33] L. Chaput, A. Togo, I. Tanaka, and G. Hug, Phonon-phonon interactions in transition metals, Phys. Rev. B **84,** 094302 (2011).

[34] S. Nosé, A unified formulation of the constant temperature molecular dynamics methods, J. Chem. Phys. **81,** 511 (1984).

[35] W. G. Hoover, Canonical dynamics: Equilibrium phase-space distributions, Phys. Rev. A **31,** 1695 (1985).

[36] M. E. Kilic and K.-R. Lee, Novel two-dimensional tetra-hexagonal boron nitride with a sizable band gap and a sign-tunable Poisson's ratio, Nanoscale **13,** 9303 (2021).

[37] V. Vierimaa, A. V. Krasheninnikov, and H.-P. Komsa, Phosphorene under electron beam: From monolayer to one-dimensional chains, Nanoscale **8,** 7949 (2016).

[38] C. Kamal and M. Ezawa, Arsenene: Two-dimensional buckled and puckered honeycomb arsenic systems, Phys. Rev. B **91,** 085423 (2015).

[39] O. Ü. Aktürk, V. O. Özçelik, and S. Ciraci, Single-layer crystalline phases of antimony: Antimonenes, Phys. Rev. B **91,** 235446 (2015).

[40] G. Li, Y. Li, H. Liu, Y. Guo, Y. Li, and D. Zhu, Architecture of graphdiyne nanoscale films, Chem. Commun. **46,** 3256 (2010).

[41] C. A. Marianetti and H. G. Yevick, Failure Mechanisms of Graphene under Tension, Phys. Rev. Lett. **105,** 245502 (2010).

[42] M. Born and K. Huang, *Dynamical Theory of Crystal Lattices* (Oxford: Clarendon Press, New York and London, 1954).

[43] E. Cadelano, P. L. Palla, S. Giordano, and L. Colombo, Elastic properties of hydrogenated graphene, Phys. Rev. B **82,** 235414 (2010).

[44] K. N. Kudin, G. E. Scuseria, and B. I. Yakobson, $C_2F$, BN, and C nanoshell elasticity from *ab initio* computations, Phys. Rev. B **64,** 235406 (2001).

[45] M. E. Kilic and K.-R. Lee, Novel two-dimensional group-IV carbides containing $C_2$ dimers: Sizable direct band gap, high carrier mobility, and anisotropic properties for nanoelectronics, Carbon **181,** 421 (2021).

[46] F. Ersan and C. Ataca, Janus $PtX_nY_{2-n}$ (X, Y = S, Se, Te; $0 \leq n \leq 2$) Monolayers for Enhanced Photocatalytic Water Splitting, Phys. Rev. Appl. **13,** 064008 (2020).

[47] H. Lang, S. Zhang, and Z. Liu, Mobility anisotropy of two-dimensional semiconductors, Phys. Rev. B **94,** 235306 (2016).

[48] Z.-G. Shao, X.-S. Ye, L. Yang, and C.-L. Wang, First-principles calculation of intrinsic carrier mobility of silicene, J. Appl. Phys. **114,** 093712 (2013).

[49] S. Saha, T. Sinha, and A. Mookerjee, Electronic structure, chemical bonding, and optical properties of paraelectric batio 3, Phys. Rev. B **62,** 8828 (2000).

[50] H. Ehrenreich and M. H. Cohen, Self-consistent field approach to the many-electron problem, Phys. Rev. **115,** 786 (1959).

[51] E. E. Salpeter and H. A. Bethe, A relativistic equation for bound-state problems, Phys. Rev. **84,** 1232 (1951).

[52] M. Shirayama, H. Kadowaki, T. Miyadera, T. Sugita, M. Tamakoshi, M. Kato, T. Fujiseki, D. Murata, S. Hara, and T. N. Murakami, Optical Transitions in Hybrid Perovskite Solar Cells: Ellipsometry, Density Functional Theory, and Quantum Efficiency Analyses for CH3 NH3 PbI 3, Phys. Rev. Appl. **5,** 014012 (2016).

[53] Z. Jiang, Z. Liu, Y. Li, and W. Duan, Scaling Universality Between Band Gap and Exciton Binding Energy of Two-Dimensional Semiconductors, Phys. Rev. Lett. **118,** 266401 (2017).

[54] L. Drissi and F. Ramadan, Excitonic effects in GeC hybrid: Many-body Green's function calculations, Phys. E: Low-Dimens. Syst. Nanostruct. **74,** 377 (2015).